Versatile Cross-Polarization Conversion Chiral Metasurface for Linear and Circular Polarizations

Peng Fei*, Guy A. E. Vandenbosch*, Weihua Guo, Xin Wen, Di Xiong, Wei Hu, Qi Zheng, Xing Chen

Dr. P. Fei, W. Guo, Dr. X. Wen, Dr. D. Xiong, Dr. X. Chen
Science and Technology on Metrology and Calibration Laboratory, Beijing Institute of Radio Metrology and Measurement, Beijing, 100854, P. R. China
feipeng@ieee.org

Prof. G. A. E. Vandenbosch
ESAT-TELEMIC Research Division, Department of Electrical Engineering, KU Leuven, 3001, Leuven, Belgium
guy.vandenbosch@kuleuven.be

Prof. W. Hu
National Key Laboratory of Antennas and Microwave Technology, Xidian University, Xi'an 710071, P. R. China

Q. Zheng
School of Electronics and Information, Northwestern Polytechnical University, 710072, Xi'an, P.R. China

Keywords: circular polarization, cross-polarization conversion, linear polarization, polarization rotation

In this work, first the necessary conditions for a versatile cross-polarization conversion meta-atom that operates both for linear and circular cross polarizations are discussed. Based on these, a versatile chiral metasurface cross-polarization converter is proposed. The correspondence between its physical geometry and polarization domain characteristics is studied. To verify the design concept, a prototype is fabricated and measured. An effective vertical and horizontal linear cross-polarization conversion is achieved from 29.3 to 38.8 GHz (27.90%) and from 34.0 to 36.6 GHz (7.36%), respectively. Furthermore, the proposed converter also achieves circular polarization handedness rotation from 34.5 to 36.6 GHz (5.91%).

Polarization is one of the essential properties of an electromagnetic wave. Polarization manipulating and controlling devices have drawn a lot of research attention in the microwave and optical frequency regimes owing to the potential applications in satellite communication, remote sensing, radar cross-section control and imaging.[1-4] Cross-polarization converters (XPC), devices that can transform an incoming wave into its orthogonally polarized counterpart by means of reflection or transmission, are among the most studied polarization manipulating devices. Different approaches have been developed to realize transmissive cross-polarization conversion. The half-wave plate, made of birefringence materials, is conventionally used in the infrared and optical spectrum. It is rarely used at lower frequencies or in integrated applications because of its large slab thickness and size.[5] In the microwave regime, previously researchers have employed waveguide phase changers, wire gratings, and meander-line grids to realize desired linear polarization (LP) or circular polarization (CP) rotation.[6-8] However, these designs usually suffer from being bulky. Recently, more sophisticated designs have been proposed. For example, a substrate integrated waveguide (SIW) structure has been used to achieve polarization rotation.[9] Orthogonal slots are etched on the opposite sides of the SIW cavity to couple the wave into and out of the cavity with the desired polarization. A class of SIW-based rotators with wide bandwidth,[10,11] conformality,[12,13] and polarization compatibility[14,15] have been reported afterwards. Another extensively studied XPC structure is based on the Fabry-Pérot cavity. Metallic wire gratings are placed perpendicular to each other on the top and bottom side of the structure, while a cut-wire array is sandwiched in the middle as the polarization rotator.[16] Modifications and improvements upon this concept have been reported to further increase the working bandwidth or achieve multi-band working properties.[17-20] Lately, the antenna-coupler-antenna (ACA) or antenna-filter-antenna (AFA) based frequency selective surfaces have been used for polarization transformation. In these structures, the unit cell is composed of a receiving antenna, a non-radiating transmission

structure, and an emitting antenna.[21] Loops,[22,23] dipoles,[24] monopoles,[25] and grids[26] are employed as the receiving/emitting antennas in these designs. In the past decade, chiral metasurfaces (CMS), which show circular dichroism, asymmetric transmission and polarization rotation in the polarization domain,[27-29] have attracted an enormous study interest.[30-34] Various types of meta-atoms (unit cells), for instance, the cross slot,[30] the via connected double-layer slot,[35] the V-shaped slot,[36] the Z-shaped resonator,[37] the T-shaped resonator,[38] the electric field-coupled resonator,[39,40] the split ring resonator[41-44] and the split-ring spiral[45] have been reported and implemented in the design of XPCs. Due to the high Q nature of CMS, such devices usually function in a limited bandwidth.

Most of the reported XPCs realize polarization rotation only if the incident wave is polarized in a very specific way. Versatile XPCs with multiple polarization states compatibility, which will provide more flexibility in practical applications, are highly demanded. Wang et al. proposed a cavity-based linear polarizer immune to the polarization direction of an incident plane wave.[14] However, the output polarization is designed to be fixed. In other words, the device will not rotate the incident wave's polarization when it is parallel with the fixed output one. A class of C4 symmetrical XPCs inspired by the concepts of ACA/AFA[24,25] and CMS[39,40,46] have been proposed. The C4 rotation symmetry allows them to transform arbitrarily directed planar LP waves into their orthogonal counterpart. Unfortunately, this is not valid for CP states.

In this communication, a novel chiral meta-atom with polarization converting properties is presented. As shown in **Figure 1**, a versatile XPC compatible with multiple polarization states is built based on this meta-atom. The structure is composed of two metallic layers and a substrate layer with a thickness less than 0.1 wavelength, which can be easily fabricated with conventional PCB technology. The proposed design shows independent polarization selecting and converting behavior for vertical and horizontal polarizations, which can be adjusted independently by changing corresponding physical parameters. Thanks to such unique

characteristics, in the overlapped passband of vertical and horizontal cross-polarization conversion, CP rotation (right-handed (RHCP) to left-handed (LHCP) and vice versa) with high conversion efficiency and low loss can also be realized.

CST Microwave Studio is used, and periodic boundary conditions along with Floquet ports are employed to carry out all simulations in the rest of the paper.

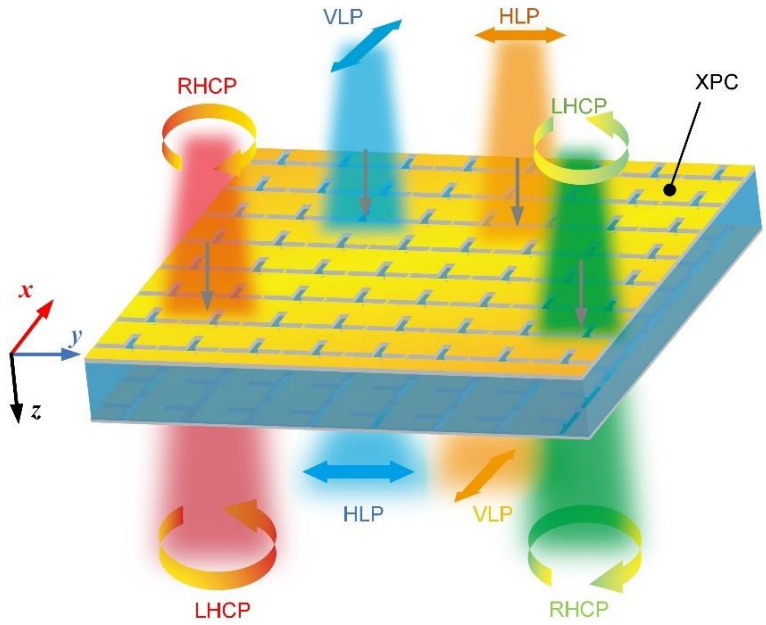

Figure 1. The working schematic of the XPC

Consider the structure in Figure 1. Assume an incident monochromatic plane wave propagating along the +*z* direction. For linear polarization, the electric field of the incident wave can be represented as

$$\boldsymbol{E}^i = \begin{bmatrix} E_x^i \\ E_y^i \end{bmatrix} \tag{1}$$

where E_x^i and E_y^i are the components in *x* and *y* directions, which are labeled as VLP (vertical linear polarization) and HLP (horizontal linear polarization), respectively. After the incident wave passes through the XPC, the transmitted electric field $\boldsymbol{E}^t$ can be written as

$$\boldsymbol{E}^t = \begin{bmatrix} E_x^t \\ E_y^t \end{bmatrix} = \boldsymbol{T} \cdot \boldsymbol{E}^i = \begin{bmatrix} T_{xx} & T_{xy} \\ T_{yx} & T_{yy} \end{bmatrix} \begin{bmatrix} E_x^i \\ E_y^i \end{bmatrix} \tag{2}$$

where $\boldsymbol{T}$ is the Jones Matrix for the LP state. T_{xx} and T_{yy} are the co-polarization transmission coefficients, and T_{yx} and T_{xy} are the cross-polarization transmission coefficients, of VLP and HLP, respectively. It is obvious that for a linear XPC, the cross-polarization transmission coefficients (T_{yx} and T_{xy}) cannot all be zero.

The Jones matrix for CP states is $\boldsymbol{T_{circ}}$, which can be written as

$$\boldsymbol{T}_{\mathbf{circ}} = \begin{bmatrix} T_{++} & T_{+-} \\ T_{-+} & T_{--} \end{bmatrix} \tag{3}$$

where T_{++} and T_{--} represent the co-polarization transmission coefficients of RHCP and LHCP, respectively, while T_{-+} and T_{+-} represent the cross-polarization transmission coefficients of RHCP and LHCP, respectively. $\boldsymbol{T_{circ}}$ can be further expressed in terms of T_{xx}, T_{xy}, T_{yx} and T_{yy} as [37,47]

$$\boldsymbol{T}_{\mathbf{circ}} = \frac{1}{2}\begin{bmatrix} T_{xx} + T_{yy} + i(T_{xy} - T_{yx}) & T_{xx} - T_{yy} - i(T_{xy} + T_{yx}) \\ T_{xx} - T_{yy} + i(T_{xy} + T_{yx}) & T_{xx} + T_{yy} - i(T_{xy} - T_{yx}) \end{bmatrix} \tag{4}$$

According to Equation 4, perfect circular XPC can be achieved when the main diagonal elements are zero while the anti-diagonal elements are non-zero, i.e.

$$T_{xx} + T_{yy} = 0 \tag{5a}$$

$$T_{xy} - T_{yx} = 0 \tag{5b}$$

Most reported circular XPCs satisfy Equation 5a and 5b by means of vanishing T_{xy} and T_{yx} while equalizing the magnitude of T_{xx} and T_{yy} and tailoring their phase difference to be 180°, [22,23] i.e.

$$T_{xx} = -T_{yy} \neq 0 \tag{6a}$$

$$T_{xy} = T_{yx} = 0 \tag{6b}$$

However, such devices cannot possibly work as linear XPC at the same time because no linear cross-polarization is theoretically allowed to pass through.

Apart from the solution in Equation 6a and 6b, there is another possible way to satisfy Equation 5a and 5b, namely:

$$T_{xx} = T_{yy} = 0 \tag{7a}$$

$$T_{xy} = T_{yx} \neq 0 \tag{7b}$$

This is a solution not well discussed in literature. A device that meets the above conditions will be able to transform incoming VLP and HLP to their cross-polarization counterparts. However, the huge advantage of this solution is that it is usable for both linear and circular cross polarization converting. It is worth noting that equations 7a and 7b represent the ideal conditions. Practically, we have to consider situations where T_{xx} and T_{yy} are low in magnitude, while T_{xy} and T_{yx} are approximately equal in magnitude and phase, respectively.

To build such a converter, firstly, we propose two sub-components (SC), which can manipulate HLP and VLP, respectively. The meta-atom of the first SC, named SC_A is composed of two orthogonally oriented metallic T-shaped slots on the opposite sides of a substrate. The geometry and dimensions of the SC_A can be found in **Figure 2** (a). The simulated transmission coefficients are illustrated in Figure 2 (b). In the passband, the HLP incoming field passes through the structure and is converted into an outgoing VLP field. The surface current distributions at 35.5 GHz are illustrated in Figure 2 (c) and (d). With VLP incidence, the induced current distributions show a non-resonant pattern on both sides of the meta-atom. Most of the incident wave is reflected. In the case of HLP incidence, the induced currents are significant on the top sheet, especially around the short stub of the T-shaped slot. Strong currents are induced on the bottom sheet around the short stub owing to slot aperture coupling between the top and bottom slots. The current distribution pattern on the bottom layer is identical in magnitude but

orthogonal in direction compared with that on the top layer. Consequently, the polarization of the field is 90° rotated while passing through the SC_A.

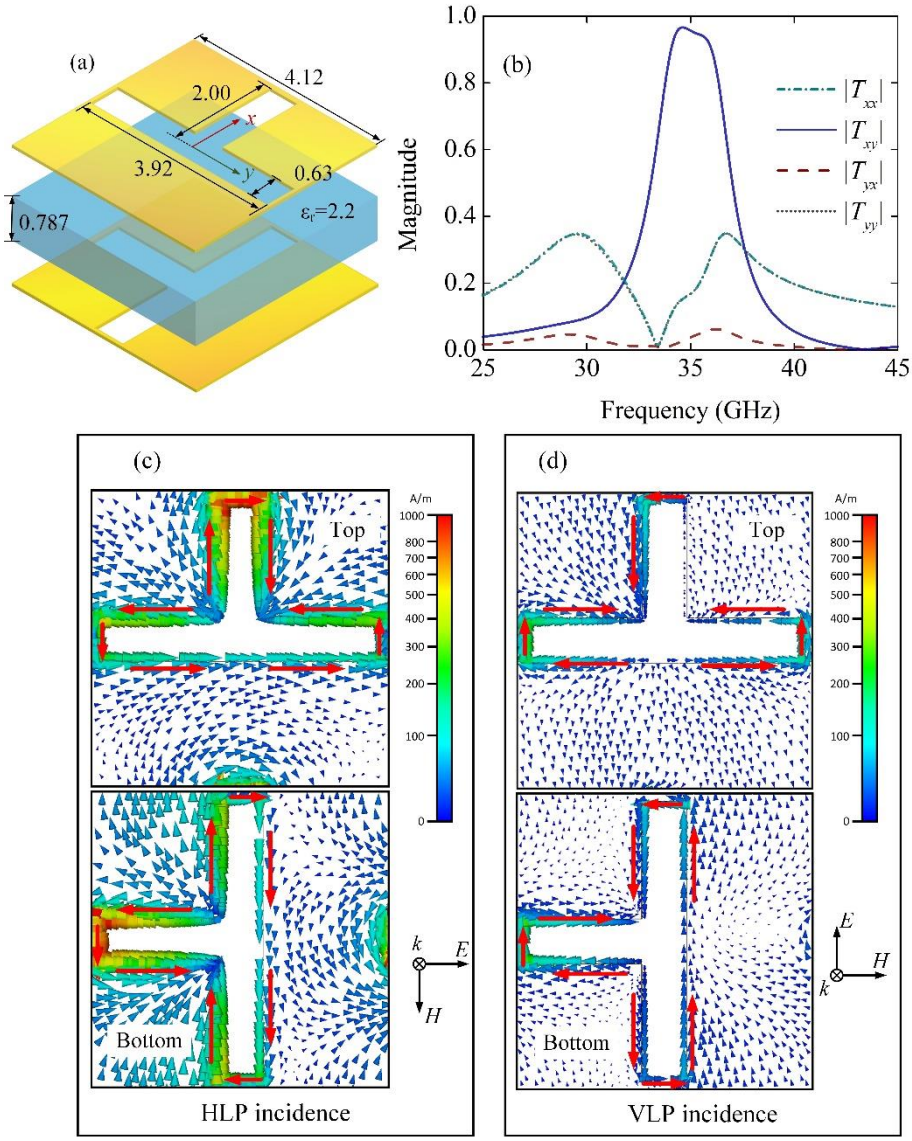

Figure 2. (a) Geometry and physical dimensions of SC_A (unit: mm); (b) transmission coefficients $|T_{xx}|$, $|T_{xy}|$, $|T_{yx}|$ and $|T_{yy}|$ of SC_A; (c) surface current distribution of SC_A with HLP incidence; (d) surface current distribution of SC_A with VLP incidence

The second SC under investigation, named SC_B, is composed of two slots orthogonally etched on the top and bottom metallic layers of substrate. The physical dimensions are shown in **Figure 3** (a). A metallic via hole located at (−0.63 mm, 0.63 mm) from the center of the meta-atom is employed to connect the top and bottom layers. Figure 3 (b) indicates that this SC_B has transmissive frequency selectivity and polarization conversion properties from 30 to 37 GHz for a VLP incident field. The surface current distributions under HLP and VLP incoming fields at 35.5 GHz are illustrated in Figure 3 (c) and (d). When an HLP field

illuminates the structure, the surface currents distribute evenly among the two sheets, with fairly inapparent concentration along the slots, suggesting that the structure functions as a reflector. However, with a VLP incident field, significant induced currents are concentrated around the ends of the slots. Also, intensive currents are observable along the via. Due to the orthogonal slot orientation, the outgoing wave, which is reradiated by the bottom slots, is rotated over 90°.

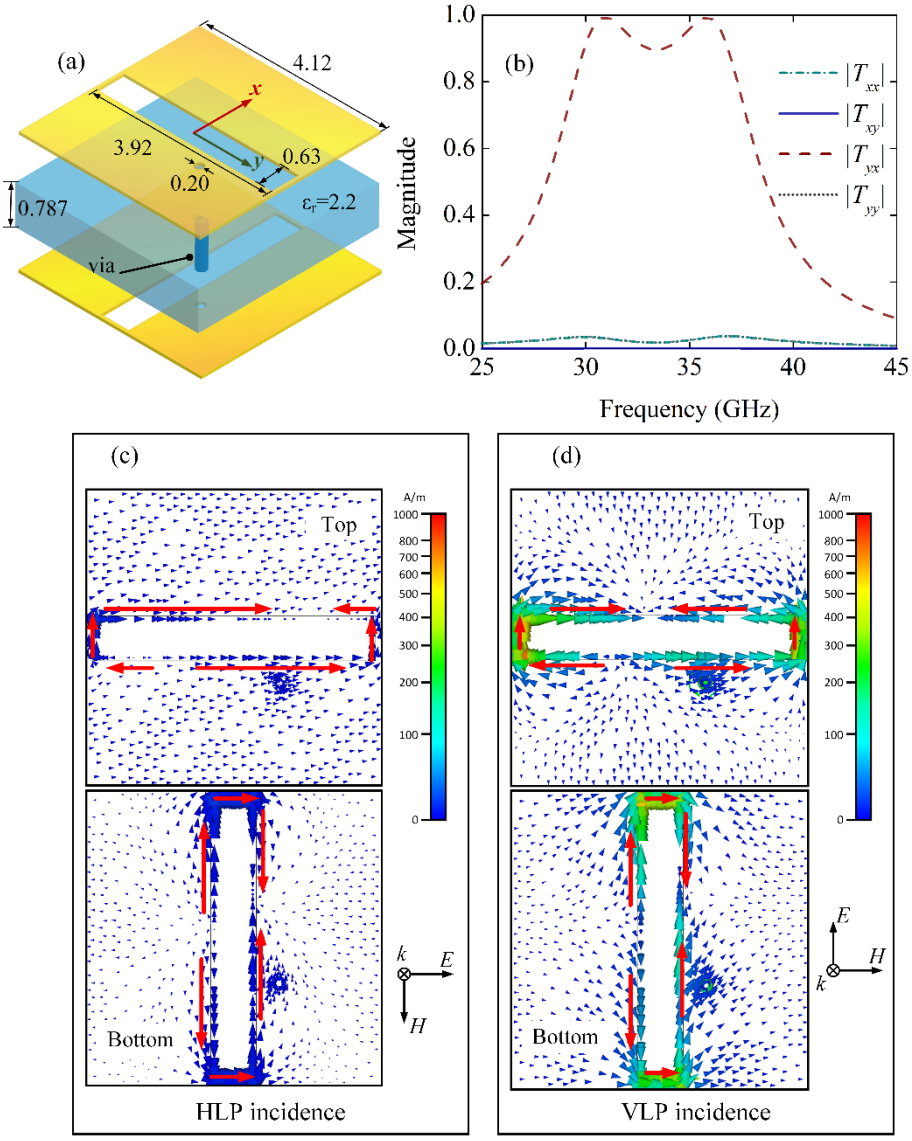

Figure 3. (a) Geometry and physical dimensions of SC_B (unit: mm); (b) transmission coefficients $|T_{xx}|$, $|T_{xy}|$, $|T_{yx}|$ and $|T_{yy}|$ of SC_B; (c) surface current distribution of SC_B with HLP incidence; (d) surface current distribution of SC_B with VLP incidence

The operation principle of both SC_A and SC_B can be explained by the ACA model. The top layer slots function as receiving antennas that take in the wave with the specific polarization, while the bottom layer slots function as emitting antennas reradiating the wave with the rotated polarization. However, the coupling mechanisms of SC_A and SC_B are different. For SC_A, the

coupling takes place in the shared slot region between the top and bottom slots by means of aperture coupling. For SC_B, the energy exchange between the layers is mainly occurring through the metallic vias. When taken separately, SC_A and SC_B only operate for HLP and VLP exclusively. However, when combining them, it is possible to obtain an XPC that does not degrade both LP converting performances. This is also based on the fact that, as shown in Figure 2 (b) and Figure 3 (b), when $|T_{xy}|$ and $|T_{yx}|$ reach near-unity, the magnitudes of $|T_{xx}|$ and $|T_{yy}|$ are low for both SC_A and SC_B. According to Equation 7a and 7b, circular-polarization conversion is possible when the phases of T_{xy} and T_{yx} are close to each other.

The combined SC_A-SC_B meta-atom of the proposed XPC is shown in **Figure 4.** The substrate used in the design has a relative permittivity ε_r = 2.2, a loss tangent tanδ = 0.0009, a thickness h = 0.787 mm, and a metal cladding thickness t = 0.017 mm. The substrate was not only chosen based on the full-wave simulation results, but also taking into account availability and machinability. The meta-atom is square in shape and placed one next to another in both x and y directions. The periods along the x and y directions are equal to the side length l. In the closely arranged metasurface, the resonant frequency is related to the period l.[28,33] In this design, l is chosen to be 4.12 mm, which is approximately equal to $\lambda_0/2$, where λ_0 is the wavelength at 35.5 GHz. T-shaped slot pairs are etched on the top and bottom metallic layers, oriented orthogonally towards each other. The width of the slot g = 0.63 mm. The lengths of the long and short slots are w and s, equal to 3.92 mm and 2.00 mm, respectively. The top and bottom metallic sheets are shorted by via holes with diameter d = 0.2 mm. The via hole is located at ($-d_x$, d_y) referenced to the center of each meta-atom, where $d_x = d_y$ = 0.63 mm. It is metalized with copper with a wall thickness of approximately 0.025 mm. The above-mentioned parameters were obtained though optimization within CST Microwave Studio.

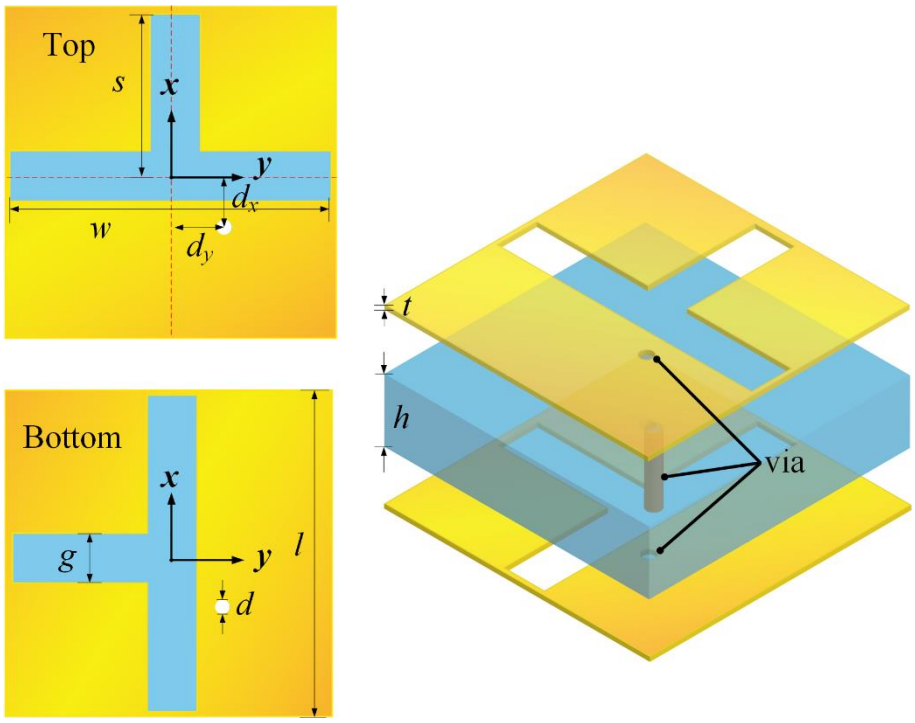

Figure 4. Geometry of the proposed XPC meta-atom

With the above-mentioned dimensions as the baseline, the performance for different short slot arm lengths *s* and long slot arm lengths *w* is studied in **Figure 5** and **Figure 6**, respectively. As shown in Figure 5 (a)-(d) and Figure 6 (a)-(d), the proposed XPC inherits the horizontal ($|T_{xy}|$) and vertical ($|T_{yx}|$) cross-polarization converting property from the SC_A and the SC_B. $|T_{xy}|$ is mainly affected by the length of the short slot arm. As *s* varies from 1.60 mm to 2.00 mm, the passband central frequency of $|T_{xy}|$ shifts from 39.3 to 35.2 GHz, while $|T_{yx}|$ is not much influenced. On the other hand, $|T_{yx}|$ is sensitive to the length of the long slot arm. As this length changes from 3.12 to 3.92 mm, the passband central frequency decreases from 40.8 to 33.8 GHz. Meanwhile, $|T_{xy}|$ is only slightly shifted to lower frequencies. Variations of $|T_{xx}|$ and $|T_{yy}|$ are also observed according to the changes of *s* and *w*. These observations are compatible with the surface current distributions depicted in **Figure 7**. HLP and VLP induced surface currents are mainly concentrated around the short and long stubs, respectively. Changing the slot length will consequently change the resonant frequency of the corresponding polarization. It is also worth to mention it can be observed from Figure 7 that the via hole region is not activated for HLP incidence. However, for VLP incidence, a significant current concentration is observed

around the via hole structure. This phenomenon further proves that the via hole is responsible for the coupling with VLP incidence. Figure 5 (e), (f) and Figure 6 (e), (f) show the magnitude difference $\Delta M=|T_{yx}| - |T_{xy}|$ and phase difference $\Delta\phi$ =arg (T_{yx}) – arg (T_{xy}) for different *s* and *w*, respectively. The circular co- and cross-polarization transmission coefficients are shown in Figure 5 (g), (h) and Figure 6 (g), (h), respectively. T_{+-} is not discussed because it has the same absolute value as T_{-+} according to Equation 4. It can be seen that T_{xy} and T_{yx} become more advanced in phase as their corresponding resonant slot decreases in length. As a result, the circular cross-polarization converting working band emerges around 35.5 GHz, when Equations 7a and 7b are approximately satisfied, i.e. when ΔM is close to 0 and $\Delta\phi$ approaches 0°, while $|T_{xx}|$ and $|T_{yy}|$ remain low in magnitude (as in the figures when *s* = 2.00 mm and *w* = 3.92 mm).

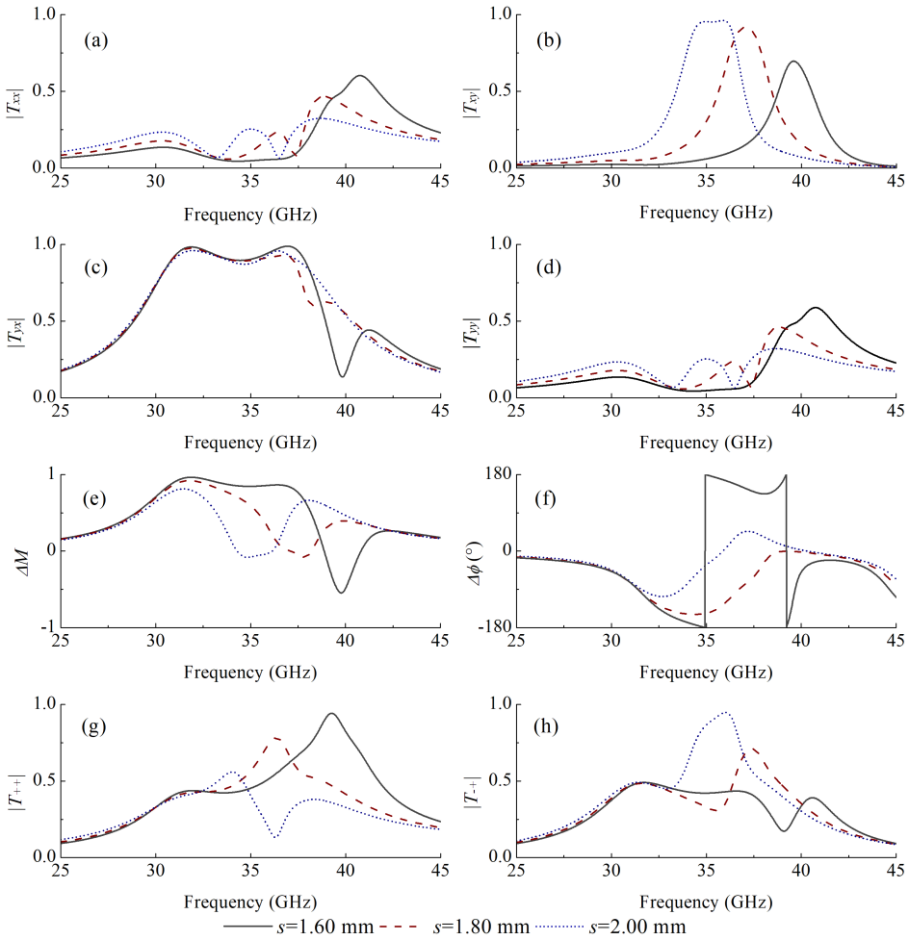

Figure 5. (a) The magnitudes of T_{xx}; (b) The magnitudes of T_{xy} ;(c) The magnitudes of T_{yx} ; (d) The magnitudes of T_{yy} ;(e) The magnitude differences between T_{yx} and T_{xy} for or different *s*; (f) The phase differences between T_{yx} and T_{xy}; (g) The magnitudes of T_{++}; and (h) The magnitudes of T_{-+}, with different short slot length *s*

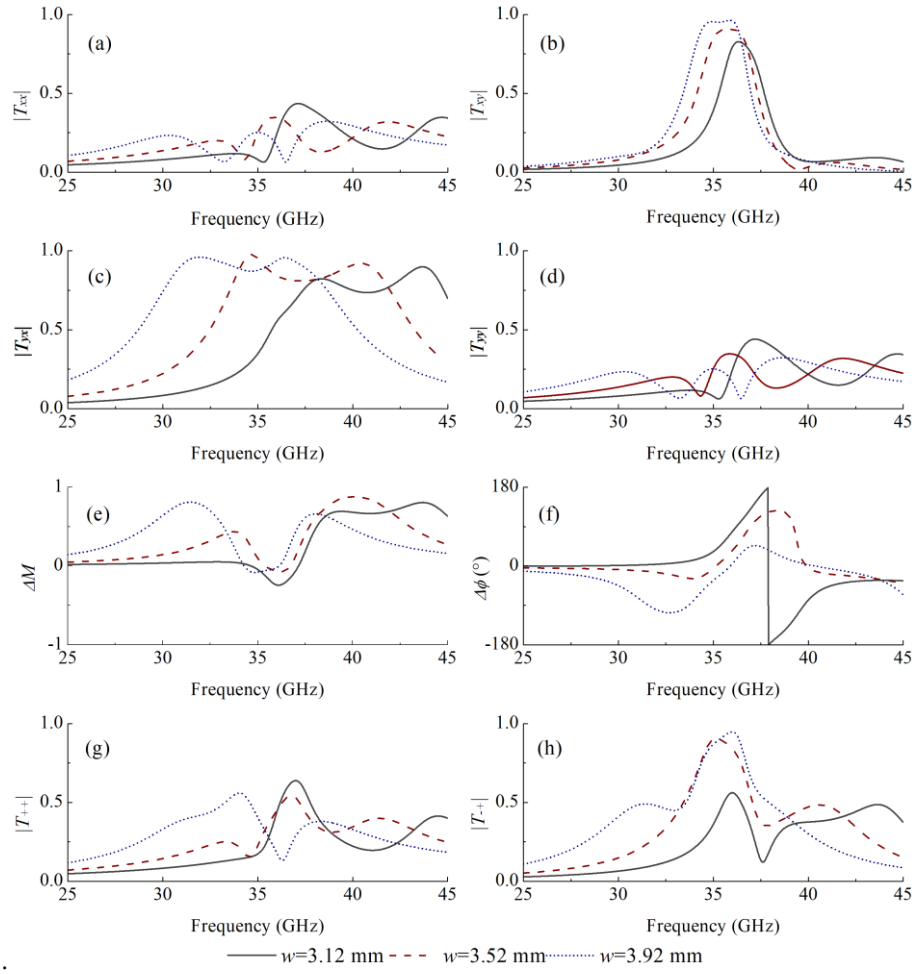

Figure 6. (a) The magnitudes of T_{xx}; (b) The magnitudes of T_{xy}; (c) The magnitudes of T_{yx}; (d) The magnitudes of T_{yy} ; (e) The magnitude differences between T_{yx} and T_{xy} for or different s; (f) The phase differences between T_{yx} and T_{xy}; (g) The magnitudes of T_{++}; and (h) The magnitudes of T_{-+}, with different long slot length w

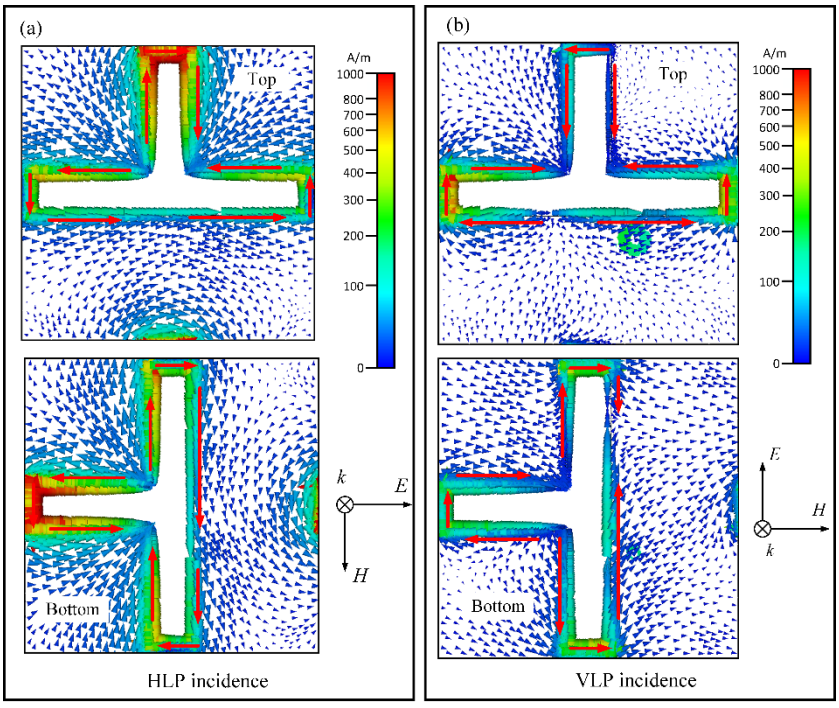

Figure 7. surface current distributions of the proposed meta-atom. (a) HLP incidence; (b) VLP incidence

Experimental Section

A prototype consisting of 45×45 meta-atoms was fabricated in order to validate the design. The area in the prototype covered by the proposed meta-atoms is about 186×186 mm^2. Commercially available Rogers RT/duroid 5880 with substrate thickness 0.787 mm and copper cladding thickness 0.017mm is employed in the fabrication. Electroless nickel/immersion gold (ENIG) is applied as surface finish. Medium-density fibreboards (MDF) with 4 mm thickness are used as supporting framework in the measurements, see **Figure 8** (a).

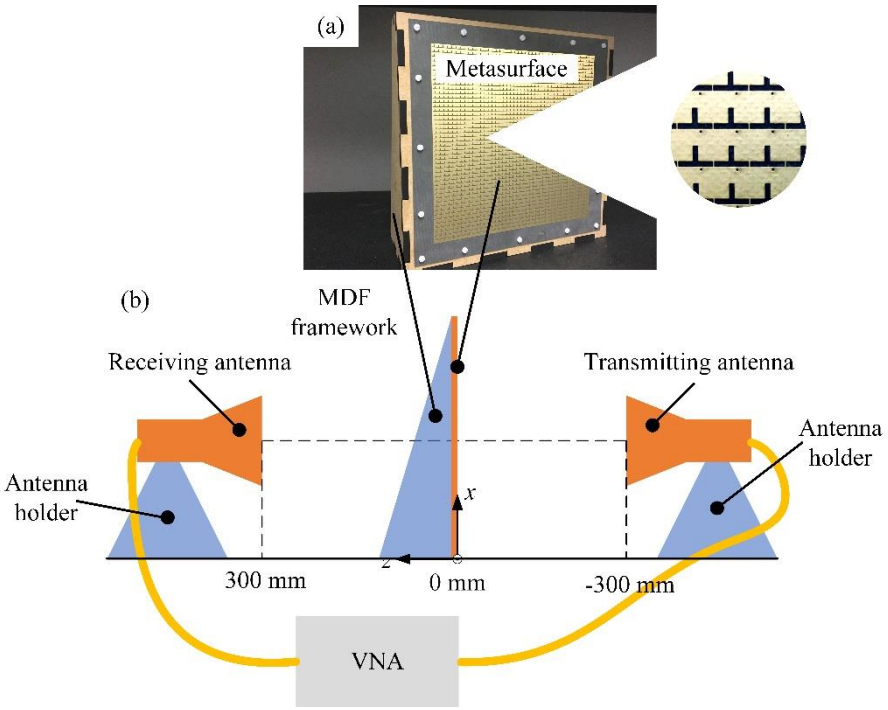

Figure 8. (a) Photograph of fabricated prototype; (b) measurement setup

The test setup is shown in Figure 8 (b). An Agilent 8510C Vector Network Analyzer (VNA) is used to record the transmission coefficient for the prototype. For linear and circular polarization, Ka-band standard pyramidal horn and conical horn antenna pairs are used respectively in the LP and CP tests. In the measurement, firstly, as shown in Figure 8(b), the transmitting and receiving antennas are placed face to face at $z = -300$ mm and $z = 300$ mm, respectively, with the same polarization. The height and position of the antennas are aligned with a laser pointer. Free space S_{21} data from 26.5 GHz to 40 GHz are recorded and calibrated.

Secondly, the prototype fixed in a wooden MDF frame is placed in the middle to keep the metasurface located in the *xoy* plane. The S_{21} data are recorded as co-polarization transmission results. Thirdly, in order to have linear polarization measurements, the receiving antenna is rotated by 90° without changing its phase center. In order to have circular polarization measurements, an antenna with opposite handedness is employed to replace the initial receiving antenna. The S_{21} data are then recorded as cross-polarization transmission results.

The raw S_{21} data contain undesired interferences from ambient reflections and multipath echoes. In order to minimize such interferences, time domain filtering is applied.[48] The recorded frequency domain S_{21} data are firstly transformed into time domain by an inverse fast Fourier transform to get the impulse response. Time domain gating is then used on this impulse to filter out echoes and unwanted reflections. After that the data are transformed back again to frequency domain by a fast Fourier transform.

The simulated and measured cross-polarization transmission coefficients are depicted in **Figure 9**. A reasonable agreement is observed. The discrepancies may be attributed to fabrication inaccuracies, calibration errors, and environmental noise. Some ripples can be observed in the measurement curves, which may be caused by the edge diffraction due to the limited prototype size. Defined on the basis of a transmission coefficient above 0.8, the working bands of $|T_{yx}|$ and $|T_{xy}|$ are 29.3 to 38.8 GHz (27.90%) and 34.0 to 36.6 GHz (7.36%), respectively. The maximum transmission coefficients for T_{yx} and T_{xy} are 0.967 and 0.953 at 36.6 GHz and 36.0 GHz, respectively. The measured circular polarization results are shown in Figure 9(b). As expected, the pass band for T_{-+} appears in the overlapped region of the T_{xy} and T_{yx} pass bands. Circular cross-polarization conversion with a transmission coefficient above 0.8 is achieved from 34.5 to 36.6 GHz (5.91%). The maximum transmission coefficient for T_{-+} is 0.942 at 36 GHz.

The polarization conversion ratio (PCR) is defined as [35,49]

$$PCR = \frac{|T_{ij}|^2}{|T_{ij}|^2+|T_{jj}|^2} \quad (8)$$

The PCRs for VLP, HLP, and LHCP incident fields, calculated based on the measured data, are shown in **Figure 10**. The measured peak values of VLP, HLP, and LHCP PCR are above 99%, indicating a very high polarization purity of the transmitted waves.

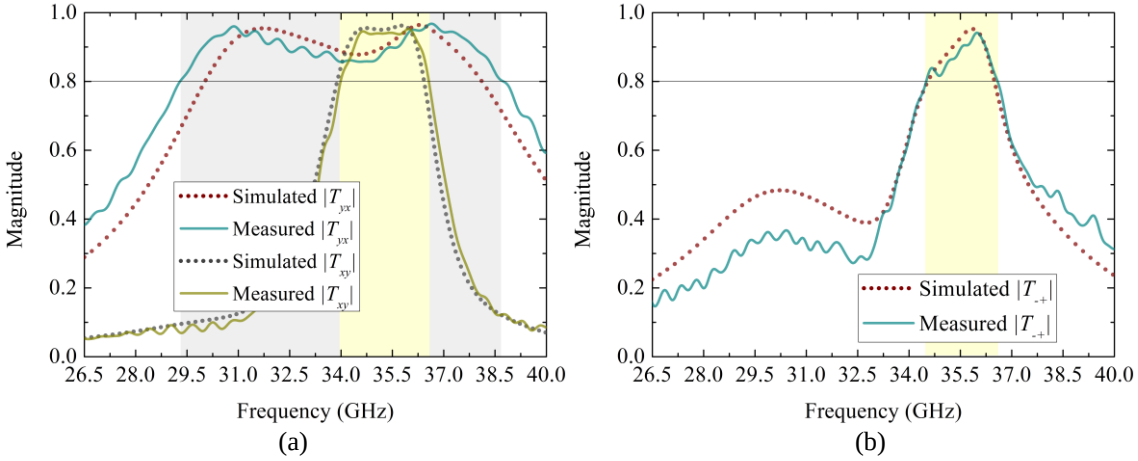

Figure 9. Simulated and measured (a) $|T_{yx}|$ and $|T_{xy}|$; (b) $|T_{-+}|$

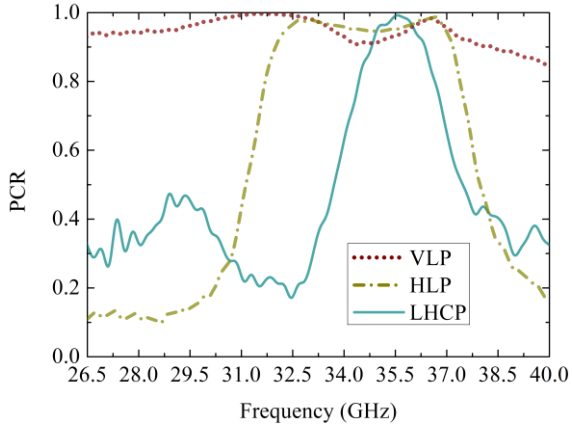

Figure 10. Measured PCR with VLP, HLP and LHCP incidence

A comparison with transmissive XPCs available in literature is given in **Table I**. All structures listed are planar with 2-3 metallic layers and operating at microwaves. It is clear that most of the reported designs can only realize polarization rotation with single LP[10,17,26,43] or CP[22,42] incident waves in a specified frequency range. In ref. [44,45], dual LP cross-polarization conversion is achieved. However, the two LP conversion passbands are completely different without any overlapped region. In ref.[32], dual LP cross-polarization conversion is realized at the same frequency. However, the working bandwidth is limited to only 4.21%, which is narrower than that of our work. C4-symmetrical chiral XPCs are reported in ref. [25,39,46]. They

can take in an arbitrarily directed LP wave and transform it into its cross-polarized counterpart. However, Jones calculus indicates that such a feature is achieved at the expense of the fact that the $|T_{-+}|$ and $|T_{+-}|$ of the C4-symmetrical chiral meta-atoms are zero, which means that they are not capable of rotating the handedness of any CP waves. To the best of our knowledge, in the whole of literature, only the work proposed by Akram et. al. is valid for both LP and CP.[37] However, it is valid for VLP, HLP, and CP cross-polarization conversion only in very limited bandwidths, which are inferior to our design. Besides, the peak transmission efficiency in ref. [37] is about 90%, which is lower compared with the one in this paper. In conclusion, the proposed XPC realizes the highest PCR in Table I. Also, it shows superiorities in efficiency, flexibility, and bandwidth compared with its peers in literature.

Table I. Comparison with literature

Category	Reference	Layers /Thickness	Polarization compatibility		Bandwidth	Peak transmission coefficient	PCR
			LP	CP			
Single LP	[10]	3/0.16λ	Single	No	28.6%	>90%	>90%
	[17]	3/0.13λ	Single	No	119.8%	>90%	Not given
	[26]	2/0.06λ	Single	No	Single narrow band	96.2%	Not given
	[43]	3/0.1λ	Single	No	24%	96%	＞99%
Dual LP	[44]	3/0.15λ	Dual	No	11.8%; >7.5%	93%	Not given
	[45]	2/0.1λ	Dual	No	≈11%; 2.5%	95%	Not given
	[32]	2/0.02λ	Dual	No	4.21%	94%	Not given
Arbitrary LP	[25]	3/0.077λ	Arbitrary	No	Single narrow band	Not given	Not given
	[39]	2/0.056λ	Arbitrary	No	Dual narrow bands	98%	96.5%
	[46]	2/0.03λ	Arbitrary	No	Dual narrow bands	Not given	Not given
CP	[22]	3/0.06λ	No	Yes	Single narrow band	97%	Not given
	[42]	2/0.06λ	No	Yes	Dual narrow bands	80%	Not given
Versatile	[37]	2/0.05λ	Dual	Yes	Single narrow band	90%	Not given
	This work	2/0.09λ	Dual	Yes	LP: 27.90%; 7.36% CP: 5.91%	LP:96.7% CP:94.2%	>99%

In this communication, a novel chiral meta-atom is proposed, and a versatile cross-polarization converter is built based on it. Both numerical and experimental studies are carried out to investigate the working mechanism and performance. The measured results indicate that

the proposed structure is capable of converting both linear and circular incident waves into their cross-polarized counterpart with extremely high efficiency.

Acknowledgements
This work is supported by National Natural Science Foundation of China (NSFC) under grant 11704037.

Received: ((will be filled in by the editorial staff))
Revised: ((will be filled in by the editorial staff))
Published online: ((will be filled in by the editorial staff))

References:

[1] Q. Zheng, C. Guo, G. A. E. Vandenbosch, P. Yuan, J. Ding, *Opt. Commun.* **2019**, *449*, 73.

[2] P. Fei, Z. Shen, X. Wen, F. Nian, *IEEE T. Antenn. Propag.* **2015**, *63*, 4609.

[3] S. Yan, G. A. E. Vandenbosch, *Appl. Phys. Lett.* **2013**, *102*, 103503.

[4] Q. Zheng, C. Guo, G. A. E. Vandenbosch, J. Ding, *IEEE Trans. Antennas Propag.* 2020, 68, 2440.

[5] F. Ding, Z. Wang, S. He, V. M. Shalaev, A. V. Kildishev, *ACS Nano* **2015**, *9*, 4111.

[6] T. Wu, *IEEE Microw. Guid. Wave Lett.* **1994**, *4*, 199.

[7] N. Amitay, A. A. M. Saleh, *IEEE T. Antenn. Propag.* **1983**, *31*, 73.

[8] A. G. Fox, *Proc. Inst. Radio Eng.* **1947**, *35*, 1489.

[9] S. A. Winkler, W. Hong, M. Bozzi, K. Wu, *IEEE T. Antenn. Propag.* **2010**, *58*, 1202.

[10] J. Wang, Z. Shen, W. Wu, *Appl. Phys. Lett.* **2016**, *109*, 153504.

[11] X. Zhu, W. Hong, K. Wu, H. Tang, Z. Hao, J. Chen, H. Zhou, H. Zhou, *IEEE T. Antenn. Propag.* **2014**, *62*, 940.

[12] K. K. Varikuntla, R. Singara Velu, *IET Microw. Antennas Propag.* **2018**, *12*, 1939.

[13] K. K. Varikuntla, R. Singara Velu, *IET Microw. Antennas Propag.* **2019**, *13*, 478.

[14] J. Wang, Z. Shen, X. Gao, W. Wu, *Opt. Lett.* **2016**, *41*, 424.

[15] M. Sharifian Mazraeh Mollaei, E. Zanganeh, R. Heydarian, F. Rangriz Rostami, S. M. Pourangha, *Int. J. RF Microw. C. E.* **2018**, *28*, e21407.

[16] N. K. Grady, J. E. Heyes, D. R. Chowdhury, Y. Zeng, M. T. Reiten, A. K. Azad, A. J. Taylor, D. A. Dalvit, H. T. Chen, *Science* **2013**, *340*, 1304.

[17] A. A. Omar, Z. Shen, S. Y. Ho, *IEEE Antennas Wirel. Propag. Lett.* **2018**, *17*, 1822.

[18] A. A. Omar, S. Ho, Z. Shen, *in Proc. 2018 Int. Conf. on Electromagnetics in Advanced Applications (ICEAA)*, IEEE, NY, 2018, 76.

[19] Y. Li, J. Zhang, S. Qu, J. Wang, L. Zheng, A. Zhang, Z. Xu, *Electron. Lett.* **2014**, *50; 50*, 1658.

[20] X. Gao, L. Singh, W. Yang, J. Zheng, H. Li, W. Zhang, *Sci. Rep.* **2017**, *7,6817*.

[21] B. Lin, J. Wu, X. Da, W. Li, J. Ma, *Appl. Phys. A* 2017, 123, 43.

[22] S. Wang, W. Liu, W. Geyi, *Appl. Phys. B* **2018**, *124*.

[23] P. Naseri, F. Khosravi, P. Mousavi, *IEEE Antennas Wirel. Propag. Lett.* **2017**, *16*, 1389.

[24] S. Wang, W. Liu, W. Geyi, *Sci. Rep.* **2018**, *8,3791*.

[25] S. Wang, W. Geyi, *in Proc. 2019 Int. Conf. on Electromagnetics in Advanced Applications (ICEAA)*, IEEE, NY, **2019**, 651.

[26] P. Xu, W. X. Jiang, S. Y. Wang, T. J. Cui, *IEEE T. Antenn. Propag.* **2018**, *66*, 4370.

[27] V. A. Fedotov, P. L. Mladyonov, S. L. Prosvirnin, A. V. Rogacheva, Y. Chen, N. I. Zheludev, *Phys. Rev. Lett.* **2006**, *97*, 167401.

[28] J. Hu, X. Zhao, R. Li, A. Zhu, L. Chen, Y. Lin, B. Cao, X. Zhu, C. Wang, *Opt. Express* **2016**, *24*, 11023.

[29] V. Y. Prinz, E. V. Naumova, S. V. Golod, V. A. Seleznev, A. A. Bocharov, V. V. Kubarev, *Sci. Rep.* **2017**, *7,43334*.

[30] X. Ma, W. Pan, C. Huang, M. Pu, Y. Wang, B. Zhao, J. Cui, C. Wang, X. Luo, *Adv. Opt. Mater.* **2014**, *2*, 945.

[31] A. A. Kirilenko, S. O. Steshenko, V. N. Derkach, S. A. Prikolotin, D. Y. Kulik, S.

Prosvirnin, L. P. Mospan, *Izv. Vyss. Uchebnykh Zaved. Radioelektron.* **2017**, *60*, 193.

[32] A. K. Baghel, S. S. Kulkarni, S. K. Nayak, *IEEE Antennas Wirel. Propag. Lett.* **2019**, *18*, 1433.

[33] S. V. Golod, V. A. Seyfi, A. F. Buldygin, A. E. Gayduk, V. Y. Prinz, *Adv. Opt. Mater.* **2018**, *6*, 1800424.

[34] B. Bai, K. Konishi, X. Meng, P. Karvinen, A. Lehmuskero, M. Kuwata-Gonokami, Y. Svirko, J. Turunen, *Opt. Express* **2009**, *17*, 688.

[35] J. M. Woo, S. Hussain, J. Jang, *Sci. Rep.* **2017**, *7*,*42952*.

[36] M. Saikia, S. Ghosh, K. V. Srivastava, *IEEE Antennas Wirel. Propag. Lett.* **2017**, *16*, 2022.

[37] M. R. Akram, M. Q. Mehmood, X. Bai, R. Jin, M. Premaratne, W. Zhu, *Adv. Opt. Mater.* **2019**, *7*, 1801628.

[38] S. Khan, T. F. Eibert, *IEEE Access* **2019**, *7*, 98045.

[39] H. Cao, H. Chen, X. Wu, Y. Pi, J. Liu, H. Xu, X. Tan, J. Lei, X. Han, *IEICE Electron. Expr.* **2016**, *13*, 20160583.

[40] H. Shi, A. Zhang, S. Zheng, J. Li, Y. Jiang, *Appl. Phys. Lett.* **2014**, *104*, 34102.

[41] X. Pan, S. Han, G. Wang, *AIP Adv.* **2014**, *4*, 97129.

[42] R. Xie, G. Zhai, X. Wang, D. Zhang, L. Si, H. Zhang, J. Ding, *Adv. Opt. Mater.* **2019**, *7*, 1900594.

[43] Z. Wei, Y. Cao, Y. Fan, X. Yu, H. Li, *Appl. Phys. Lett.* **2011**, *99*, 221907.

[44] L. Zhang, P. Zhou, H. Chen, H. Lu, H. Xie, L. Zhang, E. Li, J. Xie, L. Deng, *Sci. Rep.* **2016**, *6, 33826*.

[45] L. Wu, M. Zhang, B. Zhu, J. Zhao, T. Jiang, Y. Feng, *Appl. Phys. B* **2014**, *117*, 527.

[46] K. Song, Z. Su, M. Wang, S. Silva, K. Bhattarai, C. Ding, Y. Liu, C. Luo, X. Zhao, J. Zhou, *Sci. Rep.* **2017**, *7*.

[47] C. Menzel, C. Rockstuhl, F. Lederer, *Phys. Rev. A* **2010**, *82,053811*.

[48] B. Archambeault, S. Connor, J. C. Diepenbrock, *in Proc. 2006 Int. Symp. on Electromagnetic Compatibility (EMC2006)*, IEEE, NY, **2006**, *1*, 199.

[49] D. Liu, Z. Xiao, X. Ma, Z. Wang, *Opt. Commun.* **2015**, *354*, 272.

A versatile meta-atom is proposed and a metasurface is built based on it. Theoretical and experimental results show its versatility in converting not only the direction of linear polarization (vertical to horizontal and vice versa), but also the handedness of circular polarization (right-handed to left-handed and vice versa).

Keyword cross-polarization conversion

Peng Fei*, Guy A. E. Vandenbosch*, Weihua Guo, Xin Wen, Di Xiong, Wei Hu, Qi Zheng, Xing Chen

Title Versatile Cross-Polarization Conversion Chiral Metasurface for Linear and Circular Polarizations